

PAPER

[View Article Online](#)
[View Journal](#) | [View Issue](#)Cite this: *Dalton Trans.*, 2024, **53**, 6050

Programming heterometallic 4f–4f' helicates under thermodynamic control: the circle is complete†

Charlotte Egger,^a Laure Guénée,^b Neel Deorukhkar^a and Claude Piguet  ^{*,a}

Three non-symmetrical segmental ligand strands **L4** can be wrapped around a linear sequence of one Zn^{2+} and two trivalent lanthanide cations Ln^{3+} to give quantitatively directional $[\text{ZnLn}_2(\text{L4})_3]^{8+}$ triple-stranded helicates in the solid state and in solution. NMR speciations in CD_3CN show negligible decomplexation at a millimolar concentration and the latter helicate can be thus safely considered as a pre-organized C_3 -symmetrical $\text{HHH}-[(\text{L4}_3\text{Zn})(\text{Ln}^{\text{A}})_{(2-n)}(\text{Ln}^{\text{B}})_n]^{8+}$ platform in which the thermodynamic properties of (i) lanthanide permutation between the central N_9 and the terminal N_6O_3 binding sites and (ii) exchange processes between homo- and heterolanthanide helicates are easy to access ($\text{Ln} = \text{La}, \text{Eu}, \text{Lu}$). Deviations from statistical distributions could be programmed by exploiting specific site recognition and intermetallic pair interactions. Considering the challenging $\text{La}^{3+} : \text{Eu}^{3+}$ ionic pair, for which the sizes of the two cations differ by only 8%, a remarkable excess (70%) of the heterolanthanide is produced, together with a preference for the formation of the isomer where the largest lanthanum cation lies in the central N_9 site ($[(\text{La})(\text{Eu})] : [(\text{Eu})(\text{La})] = 9 : 1$). This rare design and its rational programming pave the way for the preparation of directional light-converters and/or molecular Q-bits at the (supra)molecular level.

Received 29th February 2024,
Accepted 29th February 2024

DOI: 10.1039/d4dt00610k

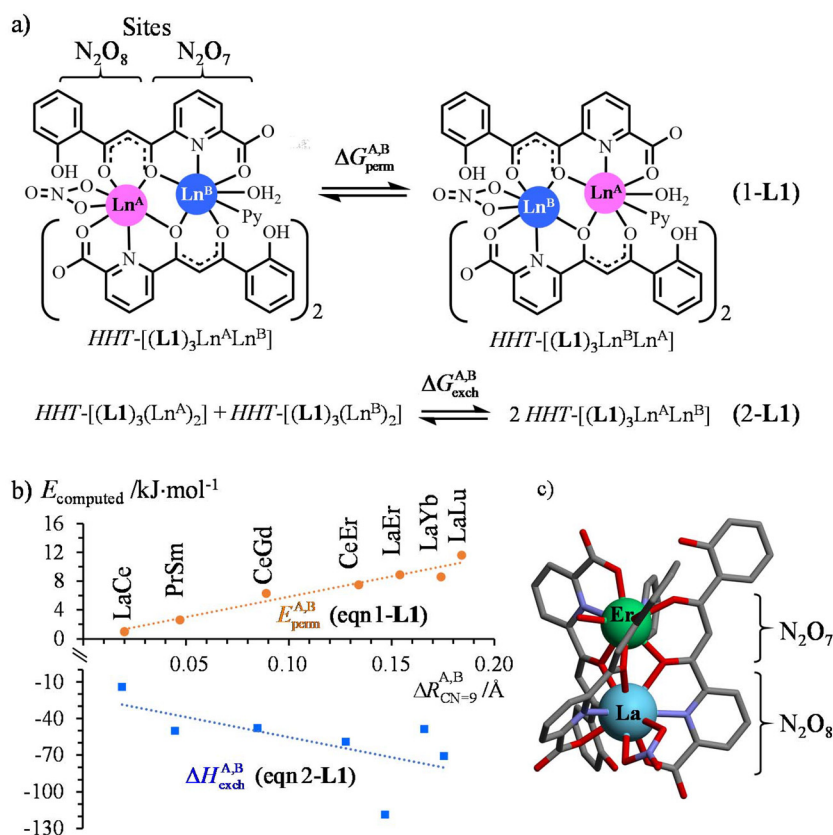
rsc.li/dalton

Introduction

The lack of radial node characterizing the atomic orbitals having $n - l = 1$ (n and l are the principal and azimuthal quantum numbers, respectively), often referred to as the primogenic effect,¹ significantly contributes to the inner-shell pseudo-atomic character of the valence 4f orbitals in the trivalent lanthanides Ln^{3+} ($[\text{Xe}]4f^n$, $n = 0-14$).²⁻⁴ The main consequence for chemistry results in a (very) similar reactivity of Ln^{3+} along the complete lanthanide series, which is only smoothly modulated by the stepwise 1% contraction of the ionic radii between adjacent elements.⁵⁻⁸ The molecular recognition of specific Ln^{3+} , beyond the standard electrostatic trend,⁵⁻⁸ is therefore mainly lacking for coordination complexes in solution.⁹ This prevents the planned design of heterometallic polynuclear f–f' assemblies in solution under thermodynamic control, except for some rare reports of deviations from statistical distributions in solution.¹⁰⁻¹⁴

Consequently, the planned implementation of pure heterometallic f–f' molecular complexes in solution mainly relies on multistep strategies which exploit the kinetic inertness provided by the complexation of Ln^{3+} within rigid, highly pre-organized and often anionic receptors (Fig. A1-1 in Appendix 1, see ESI†).¹⁵⁻²⁶ By broadening the perspective, one realizes that energy barriers, responsible for kinetic inertness, thermodynamic stability and selectivity, may greatly benefit from long-range stacking interactions accompanying crystallization processes,²⁷⁻²⁹ and serendipitous pure f–f' assemblies are therefore reported in crystalline materials (Fig. A1-2 in Appendix 1, see ESI†).^{30,31-40} The use of statistical doping has made it possible to temporarily circumvent these limits and myriads of doped ionic solids,⁴¹ nanoparticles,^{42,43} metal-organic frameworks^{30,44,45} or solid-state molecular aggregates and clusters⁴⁶⁻⁴⁹ have been prepared and explored for improving lighting and optical signaling in materials. However, the recent recognition³⁵ that the (very) minor magnetic coupling operating between two different lanthanide Kramer's ions in non-statistical molecular heterometallic f–f' entities represents a keystone for the design of basic information units in quantum computers, that is Q-bits,⁵⁰ reactivates the efforts aiming at the preparation of pure (*i.e.* non-statistical) heterometallic lanthanide molecular complexes under thermodynamic control. With this in mind, Aromi and coworkers have developed some remarkable and versatile scaffolds

^aDepartment of Inorganic and Analytical Chemistry, University of Geneva, 30 quai E. Ansermet, CH-1211 Geneva 4, Switzerland. E-mail: Claude.Piguet@unige.ch^bLaboratory of Crystallography, University of Geneva, 24 quai E. Ansermet, CH-1211 Geneva 4, Switzerland† Electronic supplementary information (ESI) available. CCDC 2320733–2320735. For ESI and crystallographic data in CIF or other electronic format see DOI: <https://doi.org/10.1039/d4dt00610k>



Scheme 1 a) Permutation (eqn 1-L1) and exchange (eqn 2-L1) equilibria proposed for the heterometallic $HHT-[(L1)_3Ln^A Ln^B(NO_3)(H_2O)(pyridine)]$ complexes and (b) associated gas-phase DFT-computed energy changes.³⁶ $\Delta R_{\text{CN}=9}^{A,B} = R_{\text{CN}=9}^{Ln^A} - R_{\text{CN}=9}^{Ln^B}$ corresponds to the difference of nine-coordinate lanthanide ionic radii in the considered metallic pair.⁵¹ The linear trendlines are only a guide to the eye. (c) Crystal structure of $HHT-[(L1)_3LaEr(NO_3)(H_2O)(pyridine)]$.³⁵

consisting of fused didentate β -diketonate and tridentate 2,6-dipicolinate units for the formation of different binding pockets, which display size discriminating effects along the lanthanide series in the solid state, when three ligands are wrapped around two (Scheme 1)^{35–37} or more trivalent cations (Fig. A1–2d in Appendix 1, see ESI†).^{38–40}

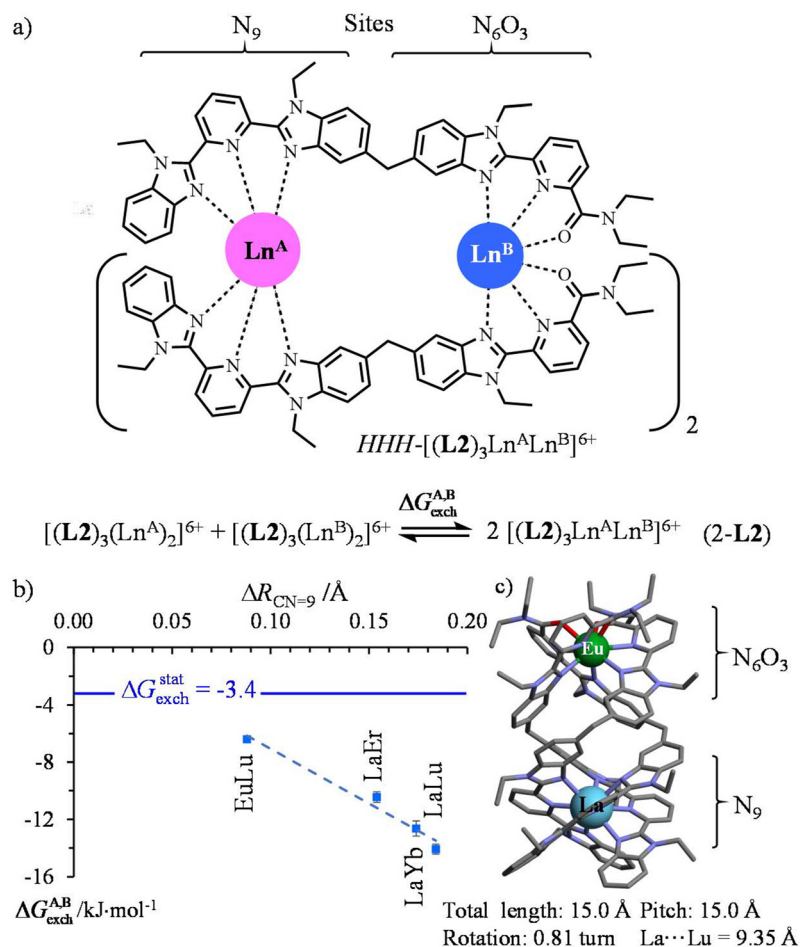
Focusing on $HHT-[(L1)_3Ln^A Ln^B(NO_3)(H_2O)(pyridine)]$,³⁶ impressive deviations ($1 \leq E_{\text{perm}}^{A,B} \leq 11 \text{ kJ mol}^{-1}$ and $-120 \leq \Delta H_{\text{exch}}^{A,B} \leq -14 \text{ kJ mol}^{-1}$, Scheme 1b) from the expected statistical distributions ($\Delta G_{\text{perm}}^{A,B,\text{stat}} = 0 \text{ kJ mol}^{-1}$ for eqn 1-L1 and $\Delta G_{\text{exch}}^{A,B,\text{stat}} = -RT \ln(4) = -3.4 \text{ kJ mol}^{-1}$ for eqn 2-L1) could be predicted by gas-phase DFT calculations assuming that the molecular structures observed in the crystalline state (Scheme 1c) are pertinent to initiate gas-phase modelling.³⁶

To the best of our knowledge, related experimental thermodynamic data are available only for homometallic/heterometallic exchange eqn (2-L2) operating in the triple-stranded $[(L2)_3(Ln^A)_{(2-n)}(Ln^B)_n]^{6+}$ helicates ($n = 0, 1, 2$) in acetonitrile (Scheme 2a).¹⁰ One can note that the measured free energy changes $-6 \leq \Delta G_{\text{exch}}^{A,B} \leq -14 \text{ kJ mol}^{-1}$ in solution (Scheme 2b) drastically differ from the optimistic gas-phase DFT-predictions reported for $HHT-[(L1)_3Ln^A Ln^B(NO_3)(H_2O)(pyridine)]$ (Scheme 1b).³⁶

The unavoidable ligand permutation, which interconverts C_3 -symmetrical $HHH-[(L2)_3(Ln^A)_{(2-n)}(Ln^B)_n]^{6+}$ with its C_1 -symmetrical $HHT-[(L2)_3(Ln^A)_{(2-n)}(Ln^B)_n]^{6+}$ counterpart, severely limits further thermodynamic analysis and the target (trivial) lanthanide exchange process involving two well-defined and different binding sites proposed by Aromi in eqn (1-L1) for $HHT-[(L1)_3Ln^A Ln^B(NO_3)(H_2O)(pyridine)]$ (Scheme 1) escaped quantification in solution with L2.

Connecting the three strands to a non-labile tripod seems to be the obvious choice for avoiding ligand scrambling and permutation, but structural constraints imposed by the helical wrapping of the strands required considerable synthetic efforts and delicate chemical design, which have been only approached once for the preorganized heterometallic dinuclear C_3 -symmetrical $[L3LaLu]^{6+}$ podate (Scheme 3a).^{52–55} The free energy change estimated for the searched La : Lu permutation summarized in eqn (1-L3) amounts to $\Delta G_{\text{perm}}^{La,Lu} = 12.1(1) \text{ kJ mol}^{-1}$ (CD_3CN at room temperature), but it entirely relies on the assumption that the mixing rule $\Delta E_{1-2}^{\text{mix}} = \Delta E_{1-2}^{La,Lu} - \frac{1}{2}(\Delta E_{1-2}^{La,Lu} + \Delta E_{1-2}^{Lu,Lu}) = 0$ is obeyed.⁵⁶

Rejuvenated by the challenge of preparing pure f-f' complexes under thermodynamic control, which are required for the preparation of molecular magnetic Q-bits,³⁶ we have re-



Scheme 2 a) Thermodynamic exchange equilibria (eqn 2-L2) and (b) associated free energy changes of the triple-stranded $[(L2)_3(Ln^A)_{(2-n)}(Ln^B)_n]^{6+}$ helicates ($x = 0, 1, 2$) in CD_3CN at room temperature.¹⁰ Only the *HHH* isomer is shown, but mixtures of *HHH* and *HHT* isomers exist in solution. $\Delta R_{CN=9}^{AB} = R_{CN=9}^{Ln^A} - R_{CN=9}^{Ln^B}$ corresponds to the difference of nine-coordinate lanthanide ionic radii in the metallic pair.⁵¹ The dashed linear trendline is only a guide to the eye. (c) Crystal structure of $HHH-[(L2)_3LaEu](ClO_4)_6$.¹⁰

engaged the fight with the use of a terminal non-covalent $HHH-[Zn(pyridine-benzimidazole)_3]$ tripod which preorganizes the three strands for their concomitant efficient binding around two successive Ln^{3+} guests in two well-defined and different coordination sites. We therefore propose in this work to close the loop with a novel and efficient preparation of the segmental ligand **L4** so that one can access the thermodynamically self-assembled $HHH-[(L4_3Zn)Ln^ALn^B]^{8+}$ helicates for which both lanthanide permutation eqn (1-L4) and lanthanide exchange eqn (2-L4) can be deciphered in solution (Scheme 3b).⁵⁷

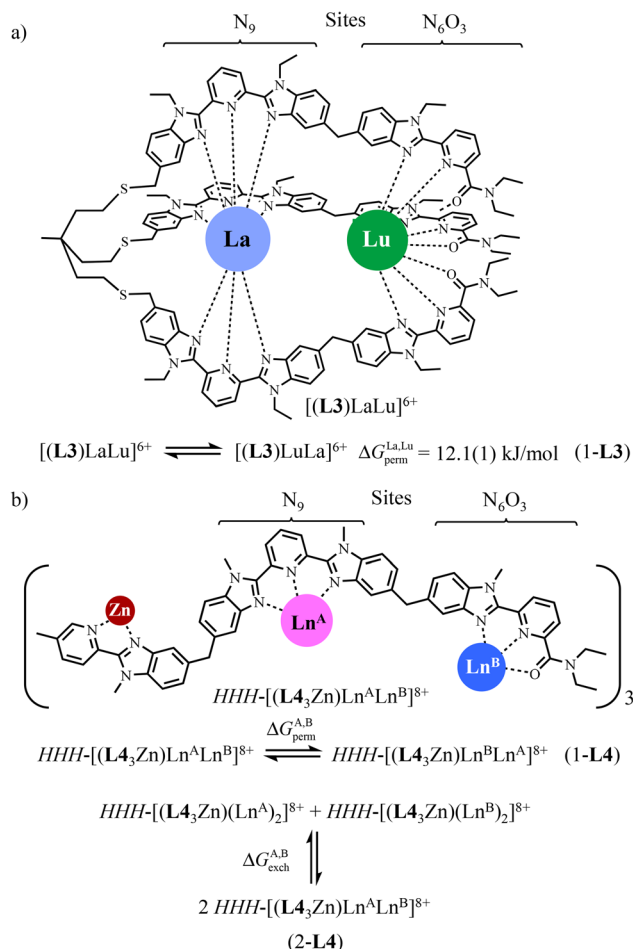
Results and discussion

Preparation and structures of **L4** and its homolanthanide triple-helical complexes $HHH-[(L4_3Zn)Ln^ALn^B]^{8+}$ ($Ln = La, Eu, Lu$)

Taking advantage of previous synthetic efforts,⁵⁷ the strategy for preparing the segmental didentate–tridentate–tridentate

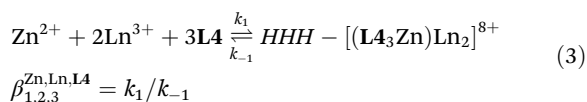
ligand **L4** has been optimized (Scheme A2-1 in Appendix 2). **L4** could be thus efficiently prepared in seven steps with a global yield of 5.6% from commercially available 2,5-lutidine (**1a**), together with previously synthesized 4,4'-methylenebis(*N*-methyl-2-nitroaniline) (**2c**),⁵⁸ 6-(diethylcarbamoyl)picolinic acid (**3d**)⁵⁹ and *N*,*N*'-diethyl-*N*'-methyl-*N*'-(4-(4-(methylamino)-3-nitrobenzyl)-2-nitrophenyl)pyridine-2,6-dicarboxamide (**8**).⁵⁹ The ¹H-NMR of the free ligand **L4** shows a total of 32 signals accounting for the 55 protons, which confirms an average *C*_s-symmetry on the NMR timescale (Fig. S1†). The absence of NOE correlations between the pyridine *meta*-protons and the benzimidazole methyl groups implies *anti* conformations of the donor N-atoms of the α,α'-diimine units, which are typical of unbound polyaromatic benzimidazole-pyridine segments in solution,^{59–61} a trend further confirmed in the crystal structure of **L4**·C₃H₈O (Fig. S2, S3 and Tables S1–S3†). The subsequent reaction of the segmental ligand **L4** (3.0 eq., 15 mM) with stoichiometric amounts of Zn(CF₃SO₃)₂ (1.0 eq., 5 mM) and Ln(CF₃SO₃)₃ (2.0 eq., 10 mM, Ln = La(III), Eu(III), Lu(III)) in CDCl₃/CD₃CN (1:2) quantitatively affords the





Scheme 3 a) Thermodynamic permutation equilibrium (eqn 1-**L3**) estimated for $[(\mathbf{L3})\text{LaLu}]^{6+}$ in CD_3CN at room temperature.⁵² b) Removal of HHH/HHT isomerism in the dinuclear-lanthanide triple-stranded helicates $\text{HHH}-[(\mathbf{L43Zn})(\text{Ln}^{\text{A}})(\text{Ln}^{\text{B}})]^{8+}$ by using $[\text{Zn}(\text{pyridine-benzimidazole})_3]$ as a preorganized non-covalent tripod.⁵⁷

target homolanthanide $\text{HHH}-[(\mathbf{L43Zn})\text{Ln}_2]^{8+}$ triple-stranded helicates within a few hours according to global equilibrium 3 (Fig. S4–S6†).



The final ^1H -NMR spectra of $\text{HHH}-[(\mathbf{L43Zn})\text{Ln}_2]^{8+}$ show the exclusive (>98%) formation of a single C_3 -symmetrical helicate in solution for each assembly process (Fig. 1 and S7–S15†). A consequence of the close vicinity of the three wrapped strands is highlighted in the diamagnetic complexes $\text{HHH}-[(\mathbf{L43Zn})\text{Ln}_2]^{8+}$ ($\text{Ln} = \text{La}, \text{Lu}$) by the unusually low chemical shifts ($4.95 \leq \delta \leq 5.85$ ppm) recorded for the aromatic protons 8, 12, 20 and 24 which are located in the shielding region of a benzimidazole ring of an adjacent strand (Fig. 1 and S7†).

One further notes that the small ionic radius of Lu(III) leads to a tighter wrapping of the ligand strands, which shifts the ^1H -NMR signals of the benzimidazole protons 8, 12, 20 and 24

from $5.07 \leq \delta \leq 5.85$ ppm in $\text{HHH}-[(\mathbf{L43Zn})\text{La}_2]^{8+}$ toward $4.95 \leq \delta \leq 5.34$ ppm in $\text{HHH}-[(\mathbf{L43Zn})\text{Lu}_2]^{8+}$ (Fig. S16 and Table S4†). The replacement of the diamagnetic La^{3+} or Lu^{3+} cations with fast-relaxing paramagnetic Eu^{3+} in $\text{HHH}-[(\mathbf{L43Zn})\text{Eu}_2]^{8+}$ results in the expected^{11,59} downfield shifts of the singlet signals of the benzimidazole protons 12, 20 and 24 ($12.00 \leq \delta \leq 14.62$ ppm) which are located close to the Eu^{3+} paramagnetic centers in the final complex (Table S5 and Fig. S8†). Additional proof for the formation of the desired complex is provided by the high-resolution ESI-TOF spectra recorded in acetonitrile, which display peaks corresponding to the series of triflate adducts $\text{HHH}-\{[(\mathbf{L43Zn})\text{Ln}_2](\text{CF}_3\text{SO}_3)_n\}^{(8-n)+}$ ($n = 2, 4, 5$; $\text{Ln} = \text{La}, \text{Eu}$), although only at low relative intensities (Fig. S17 and S19†). The theoretical isotopic patterns nicely match the experimental peaks (Fig. S18 and S20†). The rest of the peaks, which have been assigned by their isotopic patterns, correspond to partial dissociation of one or more ligand strands and/or of one or more metal ions (Tables S6 and S7†). Due to the complete lack of ^1H -NMR evidence supporting significant decomplexation of $\text{HHH}-[(\mathbf{L43Zn})\text{Ln}_2]^{8+}$ complexes ($\text{Ln} = \text{La}, \text{Eu}, \text{Lu}$) at millimolar concentrations in solution, the dissociation observed in the HR-MS spectra are assigned to the gas-phase reaction accompanying the ESI process.

Considering the labile character of both Zn(II) and Ln(III) ($\text{Ln} = \text{La}, \text{Eu}, \text{Lu}$) in solution, the formation of the desired trinuclear homolanthanide helicates within a few hours contrasts sharply with the fast (within seconds) self-assembly of the analogous dinuclear dimetallic $[\text{ZnLa}(\mathbf{6})_3]^{5+}$ complex, where the shorter segmental ligand **6** (Fig. A2–1 in Appendix 2, see ESI†) corresponds to **L4** after the removal of the central tridentate 2,6-bis(benzimidazole)pyridine unit.⁵⁹ The elongation of the ligand strand in **L4** increases the complexity of the supramolecular system, which in turn increases the number of possible intermediates and reversible steps required before converging toward the thermodynamic products.^{62,63} An ultra-simplistic consideration of the whole self-assembly process as being modeled with equilibrium (3) predicts a negligible dissociation rate constant $k_{-1} = k_1/\beta_{1,2,3}^{\text{Zn,Ln,L4}} \approx 10^{-33} \text{ h}^{-1}$ since (i) k_1 can be estimated around $1000 \text{ M}^{-6} \text{ h}^{-1}$ when one takes into account a characteristic time constant of 2 hours for the formation of 50% of the final $\text{HHH}-[(\mathbf{L43Zn})\text{Ln}_2]^{8+}$ helicate in solution at a millimolar concentration and (ii) $\log(\beta_{1,2,3}^{\text{Zn,Ln,L4}}) = 36(1)$ for $\text{HHH}-[(\mathbf{L43Zn})\text{Lu}_2]^{8+}$ in acetonitrile.⁵⁷

Slow diffusion of isopropanol and diethyl ether, respectively, into solutions of $\text{HHH}-[(\mathbf{L43Zn})\text{Eu}_2]^{8+}$ and $\text{HHH}-[(\mathbf{L43Zn})\text{La}_2]^{8+}$ in acetonitrile yielded single crystals of $[(\mathbf{L43Zn})\text{Eu}_2](\text{CF}_3\text{SO}_3)_8 \cdot 12(\text{C}_3\text{H}_8\text{O})$ and $[(\mathbf{L43Zn})\text{La}_2](\text{CF}_3\text{SO}_3)_8 \cdot 7.25(\text{CH}_3\text{CN})$ of suitable quality for X-ray diffraction analysis (Fig. 2 and S21–S28, Tables S8–S25†). The X-ray structure of analogous $[(\mathbf{L43Zn})\text{Lu}_2](\text{CF}_3\text{SO}_3)_8$ was reported previously,⁵⁷ but the limited quality of the datasets collected at this time (despite using a synchrotron radiation source) did not allow a detailed analysis of the structure.

The crystal structures unambiguously confirm the formation of the desired homolanthanide d–f–f triple-stranded helicates, showing the three metal ions almost linearly aligned



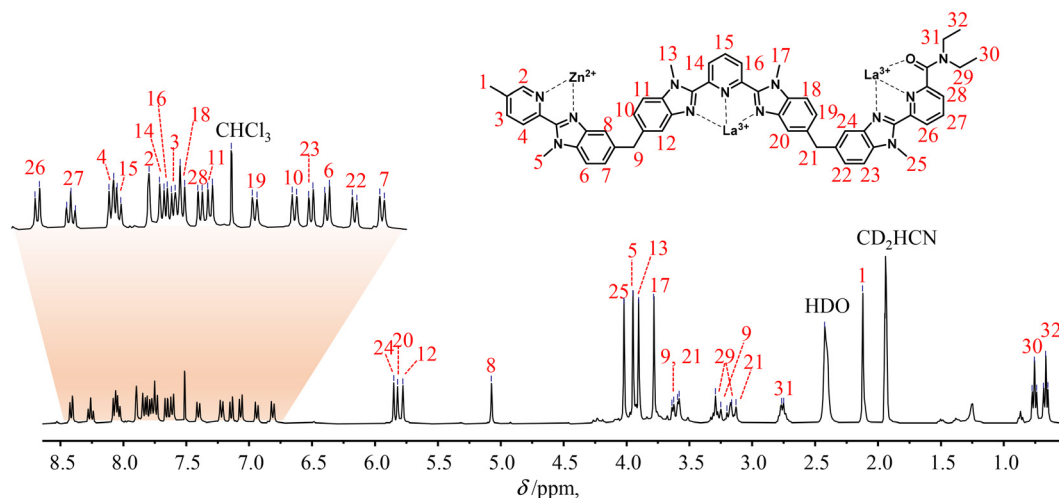


Fig. 1 ^1H -NMR spectrum of the $\text{HHH}-[(\text{L}_4\text{Zn})\text{La}_2]^{8+}$ complex (2 : 1 $\text{CD}_3\text{CN}/\text{CDCl}_3$, 400 MHz, 298 K). The aromatic region was expanded for clarity.

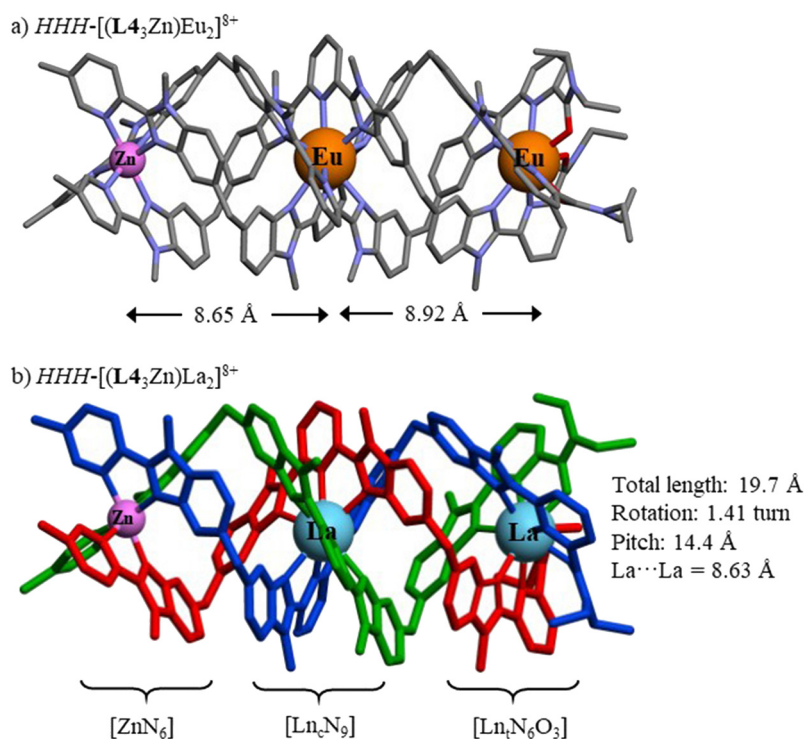


Fig. 2 Molecular structures of (a) $\text{HHH}-[(\text{L}_4\text{Zn})\text{Eu}_2]^{8+}$ as observed in the crystal structure of $[(\text{L}_4\text{Zn})\text{Eu}_2](\text{CF}_3\text{SO}_3)_8 \cdot 12(\text{C}_3\text{H}_8\text{O})$ with highlighted intermetallic distances (color code: C = grey, N = blue, O = red) and (b) $\text{HHH}-[(\text{L}_4\text{Zn})\text{La}_2]^{8+}$ as found in the crystal structure of $[(\text{L}_4\text{Zn})\text{La}_2](\text{CF}_3\text{SO}_3)_8 \cdot 7.25(\text{CH}_3\text{CN})$ with the three wrapped strands shown in different colors.

along the pseudo- C_3 axis (average $\text{Zn}-\text{Ln}_c-\text{Ln}_t$ angle $176(2)^\circ$, Fig. 2a and Table S26†) and the three ligand strands helically wrapped around them in a head-to-head-to-head fashion (Fig. 2b). The intermetallic distances between adjacent cations average to $8.7(2)$ Å (Table S26†) lie within the range of distances previously reported in a number of polynuclear lanthanide helicates based on similar *oligo*-pyridyl-benzimidazole scaffolds (Scheme 2c and Fig. 3).^{10,59,64–68} The tighter wrap-

ping of the ligand strands around the smallest lanthanide ions, previously mentioned when discussing the large upfield shift of the ^1H -NMR signals of the benzimidazole protons in $\text{HHH}-[(\text{L}_4\text{Zn})\text{Lu}_2]^{8+}$ (Fig. S16†), leads to increasingly longer intermetallic distances as the size of the coordinated lanthanide ions reduces (entries 1 and 2 in Table S26†). While the average helical pitches (14.1 – 14.4 Å) do not vary significantly between the three complexes (entry 8 in Table S26†), and



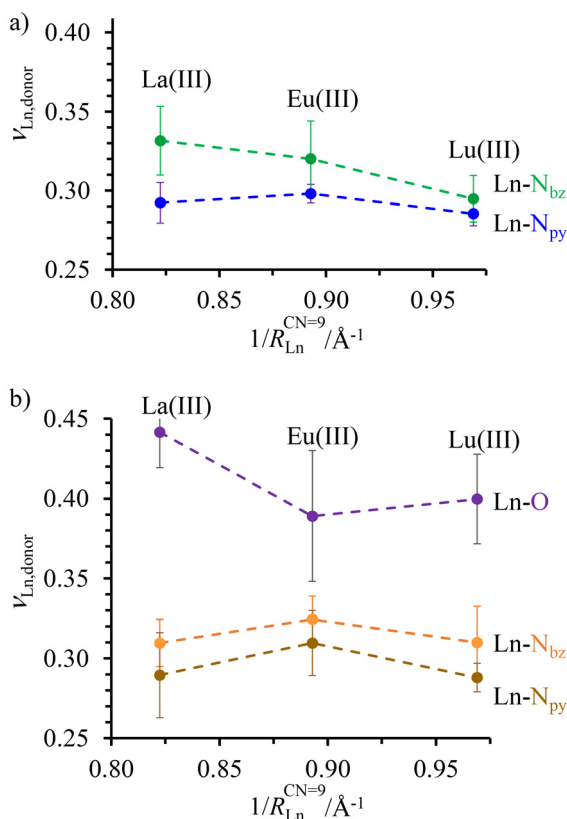


Fig. 3 Variation of the average bond valences $\nu_{\text{Ln-donor}}$ calculated with eqn (4) for (a) $\text{Ln(III)}_{\text{c}}$ in the central N_9 binding site and (b) $\text{Ln(III)}_{\text{t}}$ in the terminal N_6O_3 site as a function of the inverse of the nine-coordinate lanthanide ionic radii⁵¹ in $\text{HHH}[(\text{L}_4)_3\text{Zn}]\text{Ln}_2^{8+}$ ($\text{Ln} = \text{La(III)}, \text{Eu(III)}, \text{Lu(III)}$). Standard deviations of the averages are shown with vertical error bars. The dashed traces are only a guide to the eye.

closely mirror those measured for previous homolanthanide helicates (Fig. S29[†]), a detailed analysis of each helical portion defined by eight almost parallel facial planes F1–F8 (Fig. S22, S23 and S25–S28[†]) showed significant local variations of the wrapping mode (Table S25[†]). In all three helicates, the tight rotations observed around each binding site alternate with severely relaxed helical twists associated with the diphenyl-methane linkers. The helicity within the terminal $[\text{Ln}_t\text{N}_6\text{O}_3]$ binding site is the most irregular out of the three coordinating units due to the difference in angular rotation caused by the carboxamide-pyridine moiety on one side, and by the pyridine-benzimidazole motif on the other side.⁵⁹

The geometries of the coordination spheres around the three cations were analyzed with the software SHAPE,^{69–71} the final scores of which point toward a pseudo-octahedral arrangement for the $[\text{ZnN}_6]$ units (Table S26, entries 11 and 12[†]). Due to the poor stereochemical preferences of the lanthanide ions,^{72,73} comparable SHAPE scores are obtained for various geometries of the nine-coordinate Ln^{3+} sites. At the more flexible terminal $[\text{Ln}_t\text{N}_6\text{O}_3]$ sites, the lowest scores for all three lanthanides point to the tricapped trigonal prism geometry (Table S26, entries 20 and 21[†]). In the central $[\text{Ln}_c\text{N}_9]$ sites,

a tricapped trigonal prism geometry is adopted by the largest La(III) cation, while a spherical capped square antiprism geometry is observed around the smaller Eu(III) and Lu(III) cations (Table S26, entries 15 and 16[†]). One finally notices that the Zn–N bond distances do not vary significantly in the different $\text{HHH}[(\text{L}_4)_3\text{Zn}]\text{Ln}_2^{8+}$ helicates ($\text{Ln} = \text{La}, \text{Eu}, \text{Lu}$; Fig. S30[†]). This implies sufficient flexibility within the wrapped strands for overcoming significant structural constraints accompanying the lanthanide contraction along the 4f-series.

As expected for the flexible scaffold found in $\text{HHH}[(\text{L}_4)_3\text{Zn}]\text{Ln}_2^{8+}$, the Ln–N and Ln–O bond distances mirror the lanthanide contraction along the series (Fig. S30[†]),^{51,74,75} but a more detailed analysis of the Ln–N and Ln–O bond strengths, corrected for the lanthanide contraction, can be assessed by calculating the bond valences ν_{ij} with eqn (4), where R_{ij} is the bond valence parameter associated with a given set of metal ion i and donor atom j ,^{76–78} d_{ij} is the distance between the i – j pair, and $b = 0.37$ is a universal scaling constant (Fig. 3 and Table S27[†]).⁷⁹

$$\nu_{ij} = e^{[(R_{ij}-d_{ij})/b]} \quad (4)$$

The largest bond valences, diagnostic of the strongest metal–ligand affinities, were found between the lanthanides and the O-donors in the terminal N_6O_3 site (Fig. 3b). Interestingly, a sharp decrease of the $\text{Ln}_t\text{–O}$ bond valence observed when going from La(III) to Eu(III) is compensated by an increase of the $\text{Ln}_t\text{–N}_{\text{bz}}$ and $\text{Ln}_t\text{–N}_{\text{py}}$ interactions. The resulting concave trend detected for both $\text{Ln}_t\text{–N}_{\text{bz}}$ and $\text{Ln}_t\text{–N}_{\text{py}}$ bond valences in the terminal N_6O_3 site is not reproduced in the central N_9 site (Fig. 3a), where the average $\text{Ln}_c\text{–N}_{\text{bz}}$ interaction decreases regularly throughout the series while the $\text{Ln}_c\text{–N}_{\text{py}}$ interaction remains roughly constant. Altogether, the terminal N_6O_3 site exhibits a weak preference for binding mid-range Ln^{3+} while the central N_9 site penalizes the binding of the smaller lanthanides in $\text{HHH}[(\text{L}_4)_3\text{Zn}]\text{Ln}_2^{8+}$, a tendency previously established for the related $[\text{LnN}_9]$ and $[\text{LnN}_6\text{O}_3]$ sites found in the homolanthanide D_3 -symmetrical $[(\text{L}_5)_3\text{Ln}_2]^{6+}$ and $[(\text{L}_6)_3\text{Ln}_2]^{6+}$ helicates (Fig. S29[†]).⁸⁰

Formation and speciation of heterolanthanide triple-helical complexes $\text{HHH}[(\text{L}_4)_3\text{Zn}]\text{Ln}^{\text{A}}\text{Ln}^{\text{B}}^{8+}$ in solution ($\text{Ln}^{\text{A}}, \text{Ln}^{\text{B}} = \text{La}, \text{Eu}, \text{Lu}$)

The reaction of the segmental ligand **L4** (3.0 eq.) with a 1 : 1 : 1 mixture of $\text{Zn}(\text{CF}_3\text{SO}_3)_2$ (1.0 eq.), $\text{La}(\text{CF}_3\text{SO}_3)_3$ (1.0 eq.) and $\text{Eu}(\text{CF}_3\text{SO}_3)_3$ (1.0 eq.) in a 1 : 2 mixture of $\text{CDCl}_3/\text{CD}_3\text{CN}$ was followed by $^1\text{H-NMR}$ until the equilibrium was reached (Fig. S31[†]). The comparison of the $^1\text{H-NMR}$ spectrum of the final mixture with those of the free ligand **L4** and the previously characterized homolanthanide complexes $\text{HHH}[(\text{L}_4)_3\text{Zn}]\text{La}_2^{8+}$ and $\text{HHH}[(\text{L}_4)_3\text{Zn}]\text{Eu}_2^{8+}$ demonstrates the formation of a single major new species displaying the characteristic features of a C_3 -symmetric triple-stranded helicate (Fig. S32[†]). The rest of the (minor) signals correspond to the homolanthanide complexes, with no trace of the free ligand (Fig. 4). One of the two possible heterolanthanide isomers



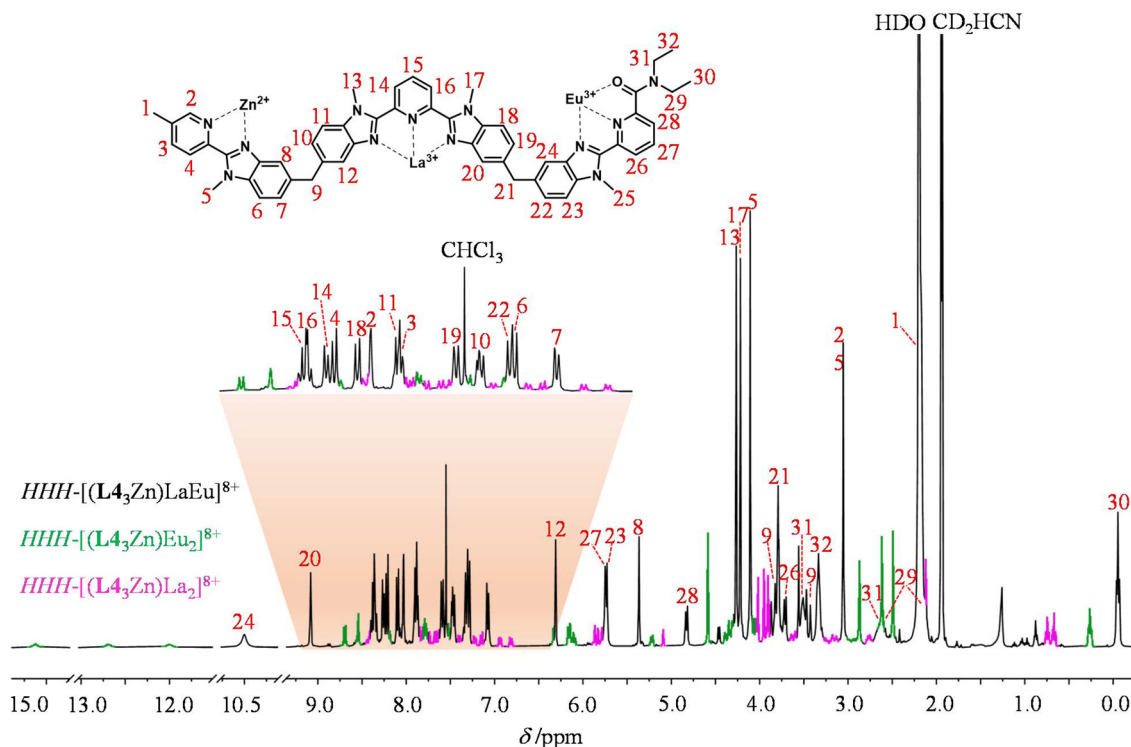


Fig. 4 ^1H -NMR spectrum of a 1:1:1:3 mixture of $\text{Zn}(\text{CF}_3\text{SO}_3)_2$, $\text{La}(\text{CF}_3\text{SO}_3)_3$, $\text{Eu}(\text{CF}_3\text{SO}_3)_3$ and **L4** at equilibrium (2:1 $\text{CD}_3\text{CN}/\text{CDCl}_3$, 400 MHz, 298 K). The aromatic region was expanded for clarity. The signals highlighted in green represent $\text{HHH}-[(\text{L}_4)_3\text{Zn}]\text{Eu}_2^{8+}$ and those in pink represent $\text{HHH}-[(\text{L}_4)_3\text{Zn}]\text{La}_2^{8+}$.

Table 1 Speciation (mole fraction) at equilibrium following the reaction of **L4** (3.0 eq., 15 mM) with a mixture of $\text{Zn}(\text{CF}_3\text{SO}_3)_2$ (1.0 eq.), $\text{Ln}^{\text{A}}(\text{CF}_3\text{SO}_3)_3$ (1.0 eq.) and $\text{Ln}^{\text{B}}(\text{CF}_3\text{SO}_3)_3$ (1.0 eq.). Thermodynamic descriptors and related free energies associated with the permutation (eqn (5)) and exchange (eqn (6)) equilibria (1:2 mixture of $\text{CDCl}_3/\text{CD}_3\text{CN}$, 298 K)

$\text{Ln}^{\text{A}}-\text{Ln}^{\text{B}}$	La-Eu	Eu-Lu	La-Lu
$\Delta R_{\text{CN}=9}^{\text{LnA}, \text{LnB}} / \text{\AA}$	0.096	0.088	0.184
$\chi(\text{HHH}-[(\text{L}_4)_3\text{Zn}]\text{Ln}^{\text{A}}]^{8+})$	0.14(1)	0.28(2)	0.25(2)
$\chi(\text{HHH}-[(\text{L}_4)_3\text{Zn}]\text{Ln}^{\text{B}}]^{8+})$	0.16(2)	0.37(4)	0.24(2)
$\chi(\text{HHH}-[(\text{L}_4)_3\text{Zn}]\text{Ln}^{\text{A}}\text{Ln}^{\text{B}}]^{8+})$	0.63(5)	0.27(3)	0.46(3)
$\chi(\text{HHH}-[(\text{L}_4)_3\text{Zn}]\text{Ln}^{\text{B}}\text{Ln}^{\text{A}}]^{8+})$	0.07(1)	0.08(1)	0.05(1)
$K_{\text{perm}}^{\text{La}_3\text{Zn}, \text{Ln}^{\text{A}}, \text{Ln}^{\text{B}}}$	0.11(2)	0.30(5)	0.11(2)
$\Delta G_{\text{perm}}^{\text{La}_3\text{Zn}, \text{Ln}^{\text{A}}, \text{Ln}^{\text{B}}} / \text{kJ mol}^{-1}$	5.4(4)	3.0(4)	5.4(5)
$K_{\text{exch}}^{\text{La}_3\text{Zn}, \text{Ln}^{\text{A}}, \text{Ln}^{\text{B}}}$	22(4)	1.2(2)	4.3(6)
$\Delta G_{\text{exch}}^{\text{La}_3\text{Zn}, \text{Ln}^{\text{A}}, \text{Ln}^{\text{B}}} / \text{kJ mol}^{-1}$	-7.5(4)	-0.4(4)	-3.6(4)
u_{1-2}^{mix}	1.4(2)	0.46(8)	0.6(1)
$\Delta E_{1-2}^{\text{mix}} / \text{kJ mol}^{-1}$	-0.8(4)	1.9(4)	1.2(5)

strongly dominates the speciation (Table 1, second column), thus confirming that the two different lanthanide binding sites exhibit size-discriminating effects. With the help of correlation and NOE spectroscopy (Fig. S33[†]), the ^1H -NMR spectrum of the main product could be fully assigned to $\text{HHH}-[(\text{L}_4)_3\text{Zn}]\text{LaEu}^{8+}$, where specific paramagnetic-induced chemical shifts (Fig. S34[†]) ascertain that the Eu(III) cation occupies

the terminal N_6O_3 binding site in the major heterolanthanide isomer (Fig. 4). As expected, the high-resolution ESI-TOF spectrum of the mixture confirmed the co-existence of both the homo- and heterolanthanide complexes in the gas-phase (Fig. S35[†]).

The formation of the $\text{HHH}-[(\text{L}_4)_3\text{Zn}]\text{LaEu}^{8+}$ complex as the main product of the self-assembly of a 1:1:1 mixture of $\text{Zn}(\text{CF}_3\text{SO}_3)_2$, $\text{La}(\text{CF}_3\text{SO}_3)_3$, and $\text{Eu}(\text{CF}_3\text{SO}_3)_3$ with 3.0 eq. of **L4** is consistent with the stereochemical preference of the central N_9 site for larger lanthanide ions and that of the terminal N_6O_3 site for smaller ones.^{10,11,80} In this context, replacing La(III) with Lu(III) in the mixture should make the coordination of the Eu(III) cation now more favorable in the central N_9 site made of three wrapped bis(benzimidazole)pyridine segments while the terminal N_6O_3 site should preferentially accommodate the smaller Lu(III), hence yielding $\text{HHH}-[(\text{L}_4)_3\text{Zn}]\text{EuLu}^{8+}$ as the major heterolanthanide isomer in solution. The latter prediction was confirmed by following the reaction of **L4** (3.0 eq., 15 mM) with a 1eq:1eq:1eq mixture of $\text{Zn}(\text{CF}_3\text{SO}_3)_2$, $\text{Eu}(\text{CF}_3\text{SO}_3)_3$ and $\text{Lu}(\text{CF}_3\text{SO}_3)_3$ in a 1:2 mixture of $\text{CDCl}_3/\text{CD}_3\text{CN}$ with the help of ^1H -NMR techniques. The ^1H -NMR spectrum recorded at equilibrium (after 24 hours, Fig. S36[†]) showed non-negligible amounts of the homolanthanide helicates $\text{HHH}-[(\text{L}_4)_3\text{Zn}]\text{Eu}_2^{8+}$ and $\text{HHH}-[(\text{L}_4)_3\text{Zn}]\text{Lu}_2^{8+}$ together with one major set of unidentified peaks that corresponded to the heterolanthanide $\text{HHH}-[(\text{L}_4)_3\text{Zn}]\text{EuLu}^{8+}$ isomer (Fig. S37–S39,† column 3 in Table 1).



Finally, the reaction of **L4** (3.0 eq., 15 mM) with a 1 eq : 1 eq : 1 eq mixture of $\text{Zn}(\text{CF}_3\text{SO}_3)_2$, $\text{La}(\text{CF}_3\text{SO}_3)_3$ and $\text{Lu}(\text{CF}_3\text{SO}_3)_3$ was the fastest to reach the equilibrium, showing little to no evolution in the ^1H -NMR spectrum after only a few hours at room temperature (Fig. S40†). Similarly to the previous mixtures, two homolanthanide helicates $\text{HHH}-[(\text{L}_4\text{Zn})\text{La}_2]^{8+}$ and $\text{HHH}-[(\text{L}_4\text{Zn})\text{Lu}_2]^{8+}$ are formed, along with only one of the two possible heterolanthanide isomers (Fig. S41–S42,† column 4 in Table 1). The absence of the open-shell $\text{Eu}(\text{III})$ probe in the mixture makes the assignment of the ^1H -NMR spectrum of the heterolanthanide $\text{HHH}-[(\text{L}_4\text{Zn})\text{LaLu}]^{8+}$ complex harder since the chemical shifts of the protons surrounding the central and the terminal sites are not as different as with the paramagnetic helicates. However, the size difference between $\text{La}(\text{III})$ and $\text{Lu}(\text{III})$ has been shown to affect the tightness of the wrapping of the ligand strands (Fig. S16†), which results in ^1H -NMR signals for the central isolated benzimidazole singlets which are diagnostic for the binding of the largest $\text{La}(\text{III})$ cation in the central N_9 site, while $\text{Lu}(\text{III})$ lies in the terminal site in $\text{HHH}-[(\text{L}_4\text{Zn})\text{LaLu}]^{8+}$ (Fig. S42†). The permuted $\text{HHH}-[(\text{L}_4\text{Zn})\text{LuLa}]^{8+}$ isomer could not be detected in the final mixture and its mole fraction was thus set at the limit of accuracy ($x \leq 0.05$) estimated for our ^1H -NMR experimental setup (Table 1).

Thermodynamic rationalization of the formation of heterolanthanide triple-helical complexes $\text{HHH}-[(\text{L}_4\text{Zn})\text{Ln}^{\text{A}}\text{Ln}^{\text{B}}]^{8+}$ in solution ($\text{Ln}^{\text{A}}, \text{Ln}^{\text{B}} = \text{La}, \text{Eu}, \text{Lu}$)

In the absence of significant complex dissociation at millimolar concentrations, as demonstrated for the stoichiometric mixing of **L4** (3.0 eq.) with $\text{Zn}(\text{CF}_3\text{SO}_3)_2$ (1.0 eq.), $\text{Ln}^{\text{A}}(\text{CF}_3\text{SO}_3)_3$ and $\text{Ln}^{\text{B}}(\text{CF}_3\text{SO}_3)_3$ (1.0 eq.) in solution, the four interconverting helicates $\text{HHH}-[(\text{L}_4\text{Zn})(\text{Ln}^{\text{A}})_{(2-n)}(\text{Ln}^{\text{B}})_n]^{8+}$ ($n = 0, 1, 2$) are related by the generic thermodynamic permutation equilibrium (1) (eqn 1–**Lk** in Schemes 1–3, further generalized below as eqn (5)) and exchange equilibrium (2) (eqn 2–**Lk** in Schemes 1–3, further generalized below as eqn (6)), where $\text{HHH}-[(\text{L}_4\text{Zn})]^{2+}$ is considered as a rigid platform for the complexation of Ln^{A} and Ln^{B} in the two appended and preorganized N_9 and N_{6O_3} binding sites (Scheme 4). The equilibrium concentrations are written between double vertical bars $||$ in eqn (5) and (6).

$$[(\text{Ln}^{\text{A}})(\text{Ln}^{\text{B}})] \rightleftharpoons [(\text{Ln}^{\text{B}})(\text{Ln}^{\text{A}})] K_{\text{perm}}^{\text{Ln}^{\text{A}}, \text{Ln}^{\text{B}}} = \frac{||(\text{Ln}^{\text{B}})(\text{Ln}^{\text{A}})||}{||(\text{Ln}^{\text{A}})(\text{Ln}^{\text{B}})||} \quad (5)$$

$$[(\text{Ln}^{\text{A}})(\text{Ln}^{\text{A}})] + [(\text{Ln}^{\text{B}})(\text{Ln}^{\text{B}})] \rightleftharpoons 2[(\text{Ln}^{\text{A}})(\text{Ln}^{\text{B}})] K_{\text{exch}}^{\text{Ln}^{\text{A}}, \text{Ln}^{\text{B}}} = \frac{||(\text{Ln}^{\text{B}})(\text{Ln}^{\text{A}})||_{\text{macro}}^2}{||(\text{Ln}^{\text{A}})(\text{Ln}^{\text{A}})|| ||(\text{Ln}^{\text{B}})(\text{Ln}^{\text{B}})||} \quad (6)$$

Focusing on $\text{HHH}-[(\text{L}_4\text{Zn})(\text{Ln}^{\text{A}})_{(2-n)}(\text{Ln}^{\text{B}})_n]^{8+}$, $K_{\text{perm}}^{\text{L}_4\text{Zn}, \text{Ln}^{\text{A}}, \text{Ln}^{\text{B}}}$ (eqn (5)) and $K_{\text{exch}}^{\text{L}_4\text{Zn}, \text{Ln}^{\text{A}}, \text{Ln}^{\text{B}}}$ (eqn (6)) can be modeled with the help of microscopic formation constants $\beta_{1,n,m}^{\text{L}_4\text{Zn}, \text{Ln}^{\text{A}}, \text{Ln}^{\text{B}}}$ to give eqn (7) and (8) within the frame of the site binding model, where $f_i^{\text{Ln}^j}$ is the intermolecular microscopic affinity of the nine-coordinate site i for the entering lanthanide Ln^j in the

preorganized $\text{HHH}-[(\text{L}_4\text{Zn})]^{2+}$ receptor and $u_{1-2}^{\text{Ln}^i, \text{Ln}^j} = \exp(-\Delta E_{1-2}^{\text{Ln}^i, \text{Ln}^j}/RT)$ is the Boltzmann factor measuring the intermetallic pair interactions $\Delta E_{1-2}^{\text{Ln}^i, \text{Ln}^j}$ operating between adjacent Ln^i and Ln^j cations in $[(\text{Ln}^i)(\text{Ln}^j)]$ (Scheme 4).^{81,82}

$$K_{\text{perm}}^{\text{L}_4\text{Zn}, \text{Ln}^{\text{A}}, \text{Ln}^{\text{B}}} = \frac{\beta_{1,1,1}^{\text{L}_4\text{Zn}, \text{Ln}^{\text{A}}, \text{Ln}^{\text{B}}}}{\beta_{1,1,1}^{\text{L}_4\text{Zn}, \text{Ln}^{\text{A}}, \text{Ln}^{\text{B}}}} = \frac{(f_{\text{N}_9}^{\text{Ln}^{\text{B}}})(f_{\text{N}_{6\text{O}_3}}^{\text{Ln}^{\text{A}}})}{(f_{\text{N}_9}^{\text{Ln}^{\text{A}}})(f_{\text{N}_{6\text{O}_3}}^{\text{Ln}^{\text{B}}})} \quad (7)$$

$$K_{\text{exch}}^{\text{L}_4\text{Zn}, \text{Ln}^{\text{A}}, \text{Ln}^{\text{B}}} = \frac{(\beta_{1,1,1}^{\text{L}_4\text{Zn}, \text{Ln}^{\text{A}}, \text{Ln}^{\text{B}}} + \beta_{1,1,1}^{\text{L}_4\text{Zn}, \text{Ln}^{\text{B}}, \text{Ln}^{\text{A}}})^2}{\beta_{1,0,2}^{\text{L}_4\text{Zn}, \text{Ln}^{\text{A}}, \text{Ln}^{\text{B}}} \cdot \beta_{1,2,0}^{\text{L}_4\text{Zn}, \text{Ln}^{\text{A}}, \text{Ln}^{\text{B}}}} = \frac{[(f_{\text{N}_9}^{\text{Ln}^{\text{A}}})(f_{\text{N}_{6\text{O}_3}}^{\text{Ln}^{\text{B}}}) + (f_{\text{N}_9}^{\text{Ln}^{\text{B}}})(f_{\text{N}_{6\text{O}_3}}^{\text{Ln}^{\text{A}}})]^2}{(f_{\text{N}_9}^{\text{Ln}^{\text{A}}})(f_{\text{N}_{6\text{O}_3}}^{\text{Ln}^{\text{A}}})(f_{\text{N}_{6\text{O}_3}}^{\text{Ln}^{\text{B}}})(f_{\text{N}_9}^{\text{Ln}^{\text{B}}})} \cdot \frac{(u_{1-2}^{\text{Ln}^{\text{A}}, \text{Ln}^{\text{B}}})^2}{u_{1-2}^{\text{Ln}^{\text{A}}, \text{Ln}^{\text{A}}} \cdot u_{1-2}^{\text{Ln}^{\text{B}}, \text{Ln}^{\text{B}}}} \quad (8)$$

The last term of eqn (8) corresponds to the square of $u_{1-2}^{\text{mix}} = (u_{1-2}^{\text{Ln}^{\text{A}}, \text{Ln}^{\text{B}}}) / (u_{1-2}^{\text{Ln}^{\text{A}}, \text{Ln}^{\text{A}}} \cdot u_{1-2}^{\text{Ln}^{\text{B}}, \text{Ln}^{\text{B}}})^{1/2}$, which is related to the mixing energy $\Delta E_{1-2}^{\text{mix}}$ in eqn (9).⁵⁶

$$\begin{aligned} \Delta E_{1-2}^{\text{mix}} &= -RT \ln(u_{1-2}^{\text{mix}}) \\ &= -RT \ln \left[\frac{(u_{1-2}^{\text{Ln}^{\text{A}}, \text{Ln}^{\text{B}}})}{(u_{1-2}^{\text{Ln}^{\text{A}}, \text{Ln}^{\text{A}}} \cdot u_{1-2}^{\text{Ln}^{\text{B}}, \text{Ln}^{\text{B}}})^{1/2}} \right] \\ &= \Delta E_{1-2}^{\text{Ln}^{\text{A}}, \text{Ln}^{\text{B}}} - \frac{1}{2} (\Delta E_{1-2}^{\text{Ln}^{\text{A}}, \text{Ln}^{\text{A}}} + \Delta E_{1-2}^{\text{Ln}^{\text{B}}, \text{Ln}^{\text{B}}}) \end{aligned} \quad (9)$$

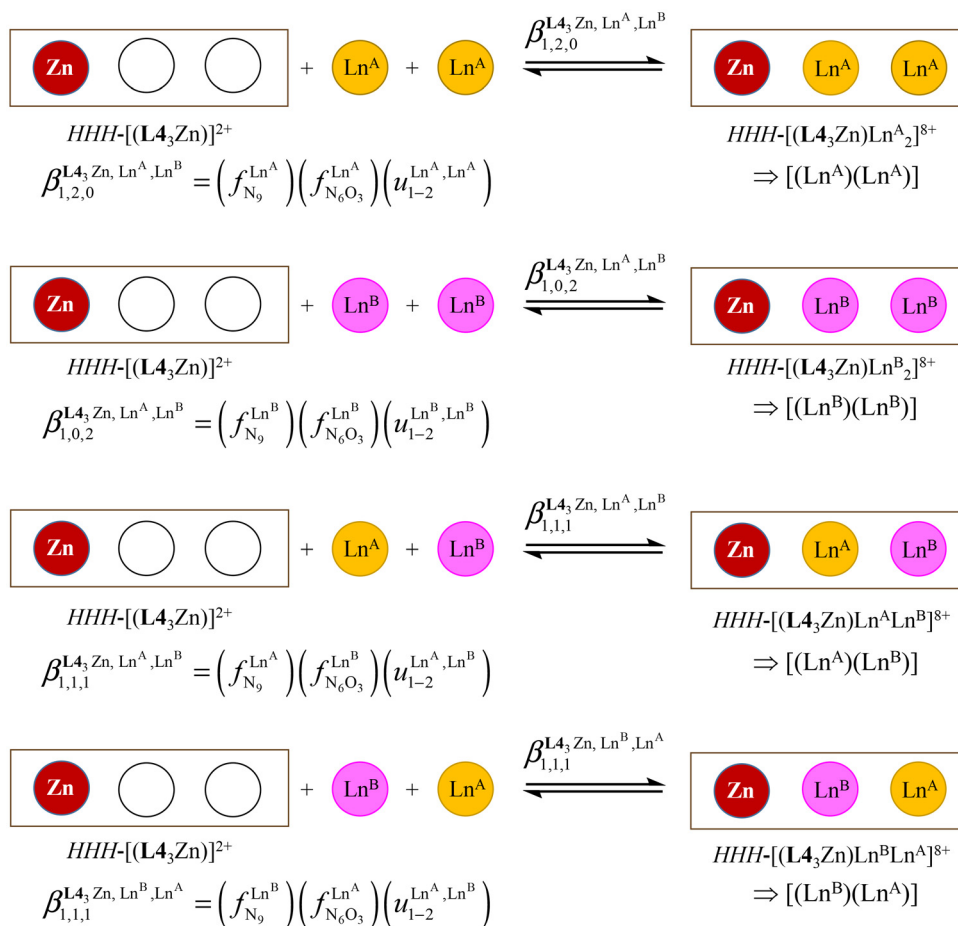
When $\Delta E_{1-2}^{\text{mix}} = 0$, the pair interaction energies obey the mixing rule $\Delta E_{1-2}^{\text{Ln}^{\text{A}}, \text{Ln}^{\text{B}}} = \frac{1}{2} (\Delta E_{1-2}^{\text{Ln}^{\text{A}}, \text{Ln}^{\text{A}}} + \Delta E_{1-2}^{\text{Ln}^{\text{B}}, \text{Ln}^{\text{B}}})$, which corresponds to a non-cooperative behavior and results in a random distribution of the two different metal ions among the coordination sites.⁵⁶ Deviations from the mixing rule can be assigned to either cooperative processes ($\Delta E_{1-2}^{\text{mix}} > 0$), which are characterized by the clustering of identical metals along the strands, or anti-cooperative processes ($\Delta E_{1-2}^{\text{mix}} < 0$), which correspond to an alternation of the different metals.^{56,81,82}

The experimental permutation energies (orange markers) and exchange energies (blue markers) obtained for $\text{HHH}-[(\text{L}_4\text{Zn})(\text{Ln}^{\text{A}})(\text{Ln}^{\text{B}})]^{8+}$ (entries 7 and 9 in Table 1) are summarized in Fig. 5. One immediately notices the systematic positive permutation energies $\Delta G_{\text{perm}}^{\text{L}_4\text{Zn}, \text{Ln}^{\text{A}}, \text{Ln}^{\text{B}}} = -RT \ln(K_{\text{perm}}^{\text{L}_4\text{Zn}, \text{Ln}^{\text{A}}, \text{Ln}^{\text{B}}}) \leq 5.6 \text{ kJ mol}^{-1}$ (top of Fig. 5), which reflect the preferred formation of the heterolanthanide isomer where the larger cation lies in the central N_9 binding site and the smaller cation occupies the terminal N_{6O_3} binding site ($K_{\text{perm}}^{\text{L}_4\text{Zn}, \text{Ln}^{\text{A}}, \text{Ln}^{\text{B}}} > 1$, eqn (7)). The combination of eqn (7) and (8), pertinent to $K_{\text{perm}}^{\text{L}_4\text{Zn}, \text{Ln}^{\text{A}}, \text{Ln}^{\text{B}}}$ and $K_{\text{exch}}^{\text{L}_4\text{Zn}, \text{Ln}^{\text{A}}, \text{Ln}^{\text{B}}}$, provides an elegant experimental access to the balance of the intermetallic pair interactions as measured by u_{1-2}^{mix} in eqn (10), and consequently to the associated mixing energies $-0.8 \leq \Delta E_{1-2}^{\text{mix}} \leq 1.9 \text{ kJ mol}^{-1}$ operating in $\text{HHH}-[(\text{L}_4\text{Zn})(\text{Ln}^{\text{A}})_{(2-n)}(\text{Ln}^{\text{B}})_n]^{8+}$ ($n = 0, 1, 2$; Table 1, entry 11).

$$K_{\text{exch}}^{\text{L}_4\text{Zn}, \text{Ln}^{\text{A}}, \text{Ln}^{\text{B}}} = \frac{(1 + K_{\text{perm}}^{\text{L}_4\text{Zn}, \text{Ln}^{\text{A}}, \text{Ln}^{\text{B}}})^2}{K_{\text{perm}}^{\text{L}_4\text{Zn}, \text{Ln}^{\text{A}}, \text{Ln}^{\text{B}}}} \cdot (u_{1-2}^{\text{mix}})^2 \quad (10)$$

When the two different lanthanide cations are larger than Gd^{3+} (= belong to the first half of the lanthanide series), as





Scheme 4 Microscopic thermodynamic formation constants $\beta_{1,j,l}^{L_4_3Zn, Ln^A, Ln^B}$ for $HHH-[(L_4_3Zn)(Ln^A)_{(2-n)}(Ln^B)_n]^{8+}$ ($n = 0, 1$, and 2) and their modeling with the site binding model.^{81,82} See main text for the definitions of $f_i^{Ln^j}$ and $u_{1-2}^{Ln^j}$.

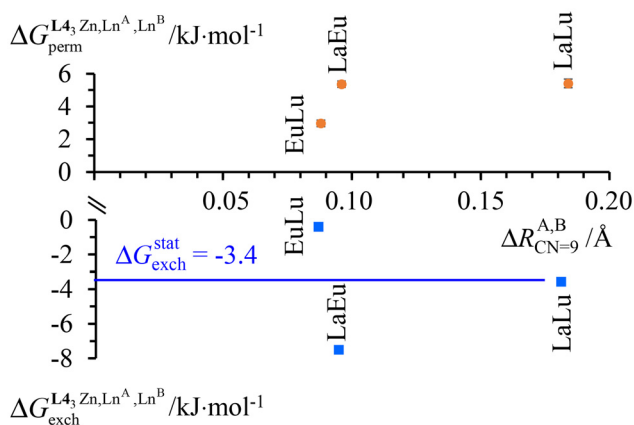


Fig. 5 Free energies for permutation ($\Delta G_{perm}^{Ln^A, Ln^B}$ in eqn (5), orange markers) and for exchange ($\Delta G_{exch}^{Ln^A, Ln^B}$ in eqn (6), blue markers) observed in solution at room temperature for $HHH-[(L_4_3Zn)(Ln^A)(Ln^B)]^{8+}$ (Table 2) as a function of the difference of the nine-coordinate lanthanide ionic radii ($\Delta R_{CN=9}^{A,B}$).⁵¹ The full traces correspond to statistical behaviours.

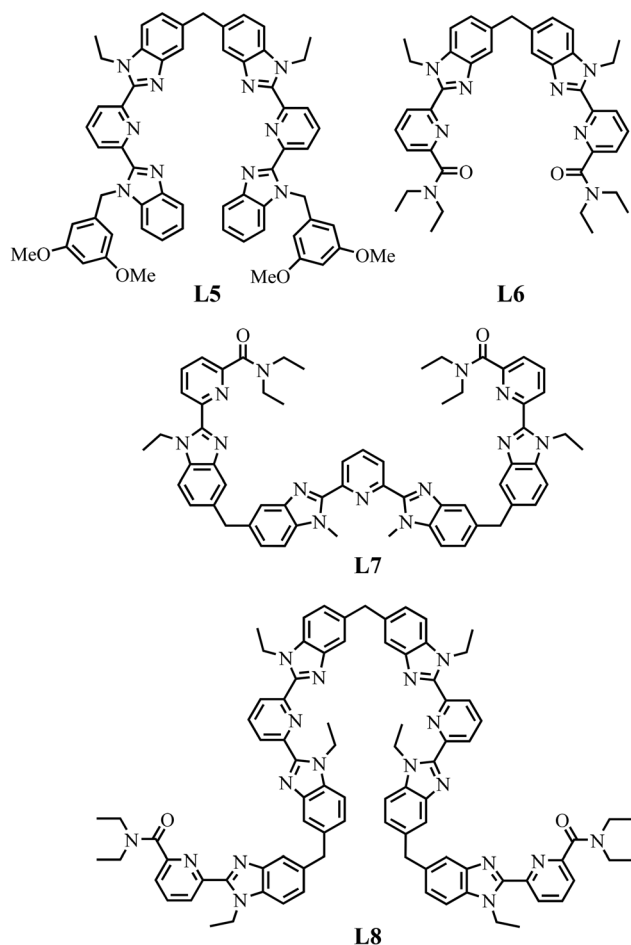
illustrated in $HHH-[(L_4_3Zn)(La)_{(2-n)}(Eu)_n]^{8+}$ ($n = 0, 1, 2$), then $\Delta E_{1-2}^{La, Eu} < \frac{1}{2}(\Delta E_{1-2}^{La, La} + \Delta E_{1-2}^{Eu, Eu})$ and the associated value of $u_{1-2}^{mix} = 1.4(2)$ boosts the formation of the heterolanthanide $HHH-$

$[(L_4_3Zn)(La)(Eu)]^{8+}$ complexes to reach $\Delta G_{exch}^{L_4_3Zn, La, Eu} = -7.5(4) \text{ kJ mol}^{-1}$, which lies much beyond the statistical value of $\Delta G_{exch}^{stat} = -RT \ln(4) = -3.4 \text{ kJ mol}^{-1}$ (bottom of Fig. 5, blue trace). As soon as one lanthanide cation of the pair belongs to the second part of the lanthanide series, as exemplified in heterolanthanide $[(Eu)(Lu)]$ and in $[(La)(Lu)]$ helicates, the reverse situation occurs with $\Delta E_{1-2}^{Ln^A, Ln^B} > \frac{1}{2}(\Delta E_{1-2}^{Ln^A, Ln^A} + \Delta E_{1-2}^{Ln^B, Ln^B})$ and the balance of pair interactions tend to discard the formation of heterolanthanide $HHH-[(L_4_3Zn)(Ln^A)(Ln^B)]^{8+}$ complexes.

The origin of the latter driving force is far from being obvious, but it can be traced back to related trends observed for the thermodynamic self-assemblies of symmetrical dinuclear $[(L_5_3)(Ln^A)_{(2-n)}(Ln^B)_n]^{6+}$ ($n = 0, 1, 2$)⁶⁵ and $[(L_6_3)(Ln^A)_{(2-n)}(Ln^B)_n]^{6+}$ ($n = 0, 1$, and 2),^{66,83} trinuclear $[(L_7_3)(Ln^A)_{(3-n)}(Ln^B)_n]^{9+}$ ($n = 0, 1, 2, 3$)¹¹ and tetranuclear $[(L_8_3)(Ln^A)_{(3-n)}(Ln^B)_n]^{12+}$ ($n = 0, 1, 2, 3$, and 4)¹² helicates (Fig. S29†) based on the segmental ligands **L5–L8** (Scheme 5, see Appendices 3–4 for a comprehensive thermodynamic analysis, see ESI†).

The two adjacent N_6O_3 binding units found in $[(L_6_3)(Ln^A)_{(2-n)}(Ln^B)_n]^{6+}$ are not able to induce deviations from statistical mixtures in solution (Fig. A3-1a in Appendix 3, see ESI†)





Scheme 5 Chemical structures of segmental ligands used for the self-assemblies of heterometallic dinuclear $[(L5_3)(Ln^A)_{(2-n)}(Ln^B)_n]^{6+}$ ($n = 0, 1, 2$)⁶⁵ and $[(L6_3)(Ln^A)_{(2-n)}(Ln^B)_n]^{6+}$ ($n = 0, 1, 2$)^{66,83} trinuclear $[(L7_3)(Ln^A)_{(3-n)}(Ln^B)_n]^{9+}$ ($n = 0, 1, 2, 3$)¹¹ and tetranuclear $[(L8_3)(Ln^A)_{(4-n)}(Ln^B)_n]^{12+}$ ($n = 0, 1, 2, 3$, and 4)¹² helicates.

and one systematically obtains $u_{1-2}^{mix} = 1$ for any lanthanide pairs ($\Delta E_{1-2}^{mix} = 0$ in Table S29†). In contrast, the two connected N_9 sites implemented in $[(L5_3)(Ln^A)_{(2-n)}(Ln^B)_n]^{6+}$ induce positive mixing energies $\Delta E_{1-2}^{mix} > \frac{1}{2}(\Delta E_{1-2}^{Ln^A, Ln^B} + \Delta E_{1-2}^{Ln^B, Ln^A})$ (Fig. A3-1b and $\Delta E_{1-2}^{mix} > 0$ in Table S28†), which favor homometallic matching beyond statistical distributions, as long as at least one lanthanide of the metallic pairs belongs to the second half of the lanthanide series. Moving from two adjacent identical nine-coordinated binding sites, as found in $[(L5_3)(Ln^A)_{(2-n)}(Ln^B)_n]^{6+}$ (N_9-N_9) or in $[(L6_3)(Ln^A)_{(2-n)}(Ln^B)_n]^{6+}$ ($N_6O_3-N_6O_3$), toward two different connected N_9 and N_6O_3 sites in $HHH-[(L4_3Zn)(Ln^A)_{(2-n)}(Ln^B)_n]^{8+}$ brings a novel dimension to the size discriminating process. Firstly, due to the presence of the central constrained N_9 site,⁸⁴ the mixing rule $\Delta E_{1-2}^{mix} > 0$ discards the formation of the heterolanthanide $HHH-[(L4_3Zn)(Ln^A)(Ln^B)]^{8+}$ isomers as soon as the small Lu^{3+} cation is considered as a member of the lanthanide pair in $[(La)(Lu)]$ and $[(Eu)(Lu)]$. Secondly, the non-zero permutation energies provided by the existence of the two different binding

Table 2 Summary of the thermodynamic free energy changes relevant to address the difference in intermolecular affinity and in intermetallic interactions which control the speciation of f-f helicates under thermodynamic control in solution beyond statistical distributions mentioned in columns 4 and 7

Helicate	Binding sites	$\Delta G_{perm}^{Ln^A, Ln^B}$ (kJ mol ⁻¹)	ΔG_{perm}^{stat} (kJ mol ⁻¹)	ΔE_{1-2}^{mix} (kJ mol ⁻¹)	$\Delta G_{exch}^{Ln^A, Ln^B}$ (kJ mol ⁻¹)	ΔG_{exch}^{stat} (kJ mol ⁻¹)	Condition	Favoured species ^a	Ref.
$[(L2)_3(Ln^A)_{(2-n)}(Ln^B)_n]^{6+}$	$N_9-N_6O_3/N_8-N_7O_2$	—	0	—	-14.1 to -6.4	-3.4	—	Hetero	10
$[(L3)_3(La)_{(2-n)}(Lu)_{(2-n)}]^{6+}$	$R-N_9-N_6O_3$	12.1	0	0 ^d	—	-3.4	—	—	52
$[(L6)_3(Ln^A)_{(2-n)}(Ln^B)_n]^{6+}$	$N_6O_3-N_6O_3$	0	0	-0.6 to 0.4	-3.5 to -3.3	-3.4	$R^{LnA} \geq R^{Gd}$ and $R^{LnB} \geq R^{Gd}$	Statistical	83
$[(L5)_3(Ln^A)_{(2-n)}(Ln^B)_n]^{6+}$	N_9-N_9	0	0	0	-3.4	-3.4	$R^{LnA} < R^{Gd}$ or $R^{LnB} < R^{Gd}$	Statistical	65
$[(L5)_3(Ln^A)_{(2-n)}(Ln^B)_n]^{6+}$	N_9-N_9	0	0	1.6 to 2.3	-0.2 to 1.2	-3.4	$R^{LnA} < R^{Gd}$ or $R^{LnB} < R^{Gd}$	Homo	65
$[(L7)_3(Ln^A)_{(3-n)}(Ln^B)_n]^{9+}$	$N_6O_3-N_9-N_6O_3$	2.2 to 4.2	3.34	-0.6 to 0.2	-10.8 to -5.4	-5.4	—	Hetero	67
$[(L8)_3(La)_{(4-n)}(Lu)_{(4-n)}]^{12+}$	$N_6O_3-N_9-N_9-N_6O_3$	—	—	-2	-47.5	-22.2	—	Hetero	12
$[(L4_3Zn)(Ln^A)_{(2-n)}(Ln^B)_n]^{8+}$	$[ZnN_6]-N_9-N_6O_3$	3.0 to 5.4	0	1.2 to 1.9	-3.6 to -0.4	-3.4	$R^{LnA} < R^{Gd}$ or $R^{LnB} < R^{Gd}$	Homo	This work
$[(L4_3Zn)(Ln^A)_{(2-n)}(Ln^B)_n]^{8+}$	$[ZnN_6]-N_9-N_6O_3$	5.4	0	-0.8	-7.5	-3.4	$R^{LnA} \geq R^{Gd}$ and $R^{LnB} \geq R^{Gd}$	Hetero	This work

^a Homo resp. hetero = preference for homometallic, resp. heterometallic lanthanide complexes; statistical = no preference. ^b The triple-stranded helicates exist as variable mixtures of HHH ($N_9-N_6O_3$) and HHT ($N_8-N_7O_2$) isomers. ^c R represents an organic tripod. ^d The mixing energy is arbitrarily fixed to $\Delta E_{1-2}^{mix} = 0$.

sites ($\text{N}_9\text{-N}_6\text{O}_3$) may partially compensate for the latter detrimental effect, and the formation of the heterolanthanide $\text{HHH}[(\text{L}_4\text{Zn})(\text{Ln}^{\text{A}})\text{Lu}]^{8+}$ isomers still represents 40–50% of the speciation in solution (Table 1, entries 4 and 5). Finally, when two large lanthanides are bound in $\text{HHH}[(\text{L}_4\text{Zn})\text{LaEu}]^{8+}$, both the balance of the intermetallic interactions ($\Delta E_{1-2}^{\text{mix}} < 0$) and site selectivity ($\Delta G_{\text{perm}}^{\text{L}_4\text{Zn,La,Eu}} > 0$) contribute favorably and synergistically to a large deviation of statistics with the formation of up to 70% of the heterolanthanide $\text{HHH}[(\text{L}_4\text{Zn})\text{LaEu}]^{8+}$ and $\text{HHH}[(\text{L}_4\text{Zn})\text{EuLa}]^{8+}$ in solution, which exist moreover in a $[(\text{La})(\text{Eu})]/[(\text{Eu})(\text{La})] = 9:1$ ratio (Table 1 and Fig. 5).

Conclusions

Puzzled by preliminary, partial and explorative studies reported for $[(\text{L}_1)_3\text{Ln}^{\text{A}}\text{Ln}^{\text{B}}(\text{NO}_3)(\text{H}_2\text{O})(\text{pyridine})]$ (Scheme 1),³⁶ $[(\text{L}_2)_3(\text{Ln}^{\text{A}})_{(2-n)}(\text{Ln}^{\text{B}})_n]^{6+}$ (Scheme 2)¹⁰ and $[(\text{L}_3)\text{LaLu}]^{6+}$ (Scheme 3),⁵² which claimed for some selective lanthanide recognition to form f-f' complexes under thermodynamic control in solution, one realizes that any pertinent discriminating effects, if they exist, should be quantitatively addressed with the help of two simple free energy descriptors measuring (i) the intermolecular affinity of a given preorganized binding site i for the entering lanthanide Ln^i ($\Delta G_{\text{aff},i}^{\text{Ln}^i} = -RT \ln(j_i^{\text{Ln}^i})$) and (ii) the balance of the intermetallic interactions operating within adjacent pairs of lanthanides $\Delta E_{1-2}^{\text{mix}} = \Delta E_{1-2}^{\text{Ln}^{\text{A}},\text{Ln}^{\text{B}}} - \frac{1}{2}(\Delta E_{1-2}^{\text{Ln}^{\text{A}},\text{Ln}^{\text{A}}} + \Delta E_{1-2}^{\text{Ln}^{\text{B}},\text{Ln}^{\text{B}}}) = -RT \ln(u_{1-2}^{\text{mix}})$.⁵⁶ Although a direct access to these two crucial thermodynamic descriptors proved to be (very) difficult,⁸⁰ an indirect approach appears to be possible since the experimentally accessible permutation equilibrium (eqn (7)), which accompanies the distribution of the various heterolanthanide isomers, and the exchange equilibrium (eqn (8)), which measures the amounts of homo- versus heterolanthanide complexes formed, reflect these thermodynamic parameters in solution. With this in mind, the lack of reliable and complete speciations addressed for the non-symmetrical $[(\text{L}_1)_3\text{Ln}^{\text{A}}\text{Ln}^{\text{B}}(\text{NO}_3)(\text{H}_2\text{O})(\text{pyridine})]$,³⁶ $[(\text{L}_2)_3(\text{Ln}^{\text{A}})_{(2-n)}(\text{Ln}^{\text{B}})_n]^{6+}$ (Table 2, entry 1)¹⁰ and $[(\text{L}_3)\text{LaLu}]^{6+}$ (Table 2, entry 2)⁵² complexes limits further rational thermodynamic analysis. In contrast, the detailed solution studies reported for the symmetrical dinuclear triple-stranded $[(\text{L}_5)_3(\text{Ln}^{\text{A}})_{(2-n)}(\text{Ln}^{\text{B}})_n]^{6+}$ and $[(\text{L}_6)_3(\text{Ln}^{\text{A}})_{(2-n)}(\text{Ln}^{\text{B}})_n]^{6+}$ helicates in solution can be used to initiate the thermodynamic exploration.⁸⁰ The strict statistical behavior observed for the loading of pairs of lanthanide cations in $[(\text{L}_6)_3(\text{Ln}^{\text{A}})_{(2-n)}(\text{Ln}^{\text{B}})_n]^{6+}$ indicates that the sequence of two adjacent semi-flexible N_6O_3 binding sites is not able to induce any significant recognition along the lanthanide series (Table 2, entry 3). The same behaviour characterizes the binding of the two large La^{3+} and Eu^{3+} cations in $[(\text{L}_5)_3(\text{La})_{(2-n)}(\text{Eu})_n]^{6+}$ (Table 2, entry 4). However, when at least one lanthanide of the pairs is smaller than Gd^{3+} , the two adjacent N_9 binding sites in the latter complexes $[(\text{L}_5)_3(\text{Ln}^{\text{A}})_{(2-n)}(\text{Ln}^{\text{B}})_n]^{6+}$ show a global preference for the formation of homometallic complexes due to cooperative intermetallic

mixing energies $\Delta E_{1-2}^{\text{mix}} \approx 2 \text{ kJ mol}^{-1}$ (Table 2, entry 5). The symmetrical trinuclear $[(\text{L}_7)_3(\text{Ln}^{\text{A}})_{(3-n)}(\text{Ln}^{\text{B}})_n]^{9+}$ ($\text{N}_6\text{O}_3\text{-N}_9\text{-N}_6\text{O}_3$, Table 2 entry 6) and tetranuclear $[(\text{L}_8)_3(\text{Ln}^{\text{A}})_{(4-n)}(\text{Ln}^{\text{B}})_n]^{12+}$ ($\text{N}_6\text{O}_3\text{-N}_9\text{-N}_9\text{-N}_6\text{O}_3$, Table 2 entry 7) helicates confirm these trends with the appearance of sizeable unbalanced intermetallic interactions (*i.e.* $\Delta E_{1-2}^{\text{mix}} \neq 0$) only when a sequence of two adjacent N_9 site binding sites exists.

When a constrained sequence of two adjacent N_6O_3 and N_9 binding sites is ensured *via* the connection of the ligand strands to a covalent sulfur tripod in $[(\text{L}_3)\text{LaLu}]^{6+}$ (Table 2, entry 2) or to a non-covalent $[\text{ZnN}_6]$ podand in the $\text{HHH}[(\text{L}_4\text{Zn})(\text{Ln}^{\text{A}})_{(2-n)}(\text{Ln}^{\text{B}})_n]^{8+}$ helicates (Table 2, entries 8 and 9), both the specific binding site affinities (*via* $\Delta G_{\text{perm}}^{\text{L}_4\text{Zn,Ln}^{\text{A}},\text{Ln}^{\text{B}}}$, eqn (7)) and the intermetallic mixing energies (*via* $\Delta G_{\text{exch}}^{\text{L}_4\text{Zn,Ln}^{\text{A}},\text{Ln}^{\text{B}}}$, eqn (8)) can be exploited for boosting the formation of one targeted heterolanthanide isomer in solution. The systematic preference of the central N_9 site for binding the largest lanthanide of the $\text{Ln}^{\text{A}}:\text{Ln}^{\text{B}}$ pair favors the formation of the heterolanthanide $\text{HHH}[(\text{L}_4\text{Zn})\text{Ln}^{\text{A}}\text{Ln}^{\text{B}}]^{8+}$ isomer when $R^{\text{Ln}^{\text{A}}} > R^{\text{Ln}^{\text{B}}}$ ($\Delta G_{\text{perm}}^{\text{L}_4\text{Zn,Ln}^{\text{A}},\text{Ln}^{\text{B}}} > 0$). However, the unfavorable mixing energy $\Delta E_{1-2}^{\text{perm}} > \frac{1}{2}(\Delta E_{1-2}^{\text{Ln}^{\text{A}},\text{Ln}^{\text{A}}} + \Delta E_{1-2}^{\text{Ln}^{\text{B}},\text{Ln}^{\text{B}}})$ accompanying the distribution of the two lanthanides within the two sites as soon as one is smaller than Gd^{3+} limits this drift with the formation of only 51% of the heterolanthanide complexes for the $\text{La}:\text{Lu}$ pair and 35% for the $\text{Eu}:\text{Lu}$ pair (Table 2, entry 8). The latter restriction is removed when the two lanthanides belong to the first half of the series as demonstrated for the challenging $\text{La}^{3+}:\text{Eu}^{3+}$ ionic pair in $\text{HHH}[(\text{L}_4\text{Zn})\text{LaEu}]^{8+}$ (Table 2, entry 9; the sizes of the two cations differ by only 8%), where the latter isomer accounts for 63% of the speciation in solution under stoichiometric conditions ($[(\text{L}_4\text{Zn})]_{\text{tot}} = [\text{La}]_{\text{tot}} = [\text{Eu}]_{\text{tot}}$). This largely exceeds the 25% predicted by the statistical distribution. The road to the selective formation of f-f' heterometallic complexes under thermodynamic control is still a long one, but the use of non-covalent tripods for programming specific sequences of binding sites, as demonstrated here for $\text{HHH}[(\text{L}_4\text{Zn})\text{Ln}^{\text{A}}\text{Ln}^{\text{B}}]^{8+}$ helicates, corresponds to a major step forward in the rational design of heterolanthanide complexes obtained under thermodynamic control.

Conflicts of interest

There are no conflicts to declare.

Acknowledgements

Financial support from the Swiss National Science Foundation is gratefully acknowledged (grant 200020_207313).

References

- 1 J. K. McCusker, *Science*, 2019, **363**, 484–488.
- 2 P. F. Lang and B. C. Smith, *J. Chem. Educ.*, 2010, **87**, 875–881.



- 3 A. J. Freeman and R. E. Watson, *Phys. Rev.*, 1962, **127**, 2058–2076.
- 4 M. G. Brik and C.-G. Ma, *Theoretical Spectroscopy of Transition Metal and Rare Earth Ions*, Jenny Stanford Publishing, Singapore, 2020, ch. 6, pp. 145–244.
- 5 R. Saez and P. Caro, *Rare Earths*, Editorial Complutense S. A., Madrid, 1998.
- 6 S. Cotton, *Lanthanide and Actinide Chemistry*, John Wiley & Sons, Ltd, 2006.
- 7 E. N. Rizkalla and G. R. Choppin, Hydration and Hydrolysis of Lanthanides, in *Handbook on the Physics and Chemistry of Rare Earths*, ed. K. A. Gschneidner, Jr and L. Eyring, Elsevier Science Publishers, 1991, vol. 15, pp. 393–442.
- 8 G. R. Choppin and E. N. Rizkalla, Solution Chemistry of Actinides and Lanthanides, in *Handbook on the Physics and Chemistry of Rare Earths*, ed. K. A. Gschneidner, Jr, L. Eyring, G. R. Choppin and G. H. Lander, Elsevier Science B.V., 1994, vol. 18, pp. 559–589.
- 9 V. S. Sastri, J.-C. Bünzli, V. R. Rao, G. V. S. Rayudu and J. R. Perumareddi, *Modern Aspects of Rare Earths and their Complexes*, Elsevier B. V., Amsterdam, 2003, ch. 3–4, pp. 127–374.
- 10 N. André, T. B. Jensen, R. Scopelliti, D. Imbert, M. Elhabiri, G. Hopfgartner, C. Piguet and J.-C. G. Bünzli, *Inorg. Chem.*, 2004, **43**, 515–529.
- 11 S. Floquet, M. Borkovec, G. Bernardinelli, A. Pinto, L.-A. Leuthold, G. Hopfgartner, D. Imbert, J.-C. G. Bünzli and C. Piguet, *Chem. – Eur. J.*, 2004, **10**, 1091–1105.
- 12 N. Dalla-Favera, J. Hamacek, M. Borkovec, D. Jeannerat, G. Ercolani and C. Piguet, *Inorg. Chem.*, 2007, **46**, 9312–9322.
- 13 A. M. Johnson, M. C. Young, X. Zhang, R. R. Julian and R. J. Hooley, *J. Am. Chem. Soc.*, 2013, **135**, 17723–17726.
- 14 L. Bellucci, L. Fioravanti, L. Armelao, G. Bottaro, F. Marchetti, F. Pineider, G. Poneti, S. Samaritani and L. Labella, *Chem. – Eur. J.*, 2022, **29**, e202202823.
- 15 J. Wahsner and M. Seitz, *Inorg. Chem.*, 2015, **54**, 9681–9683.
- 16 J. W. Buchler, A. De Cian, J. Fischer, M. Kihn-Botulinski, H. Paulus and R. Weiss, *J. Am. Chem. Soc.*, 1986, **108**, 3652–3659.
- 17 N. Ishikawa, T. Iino and Y. Kaizu, *J. Am. Chem. Soc.*, 2002, **124**, 11440–11447.
- 18 S. Faulkner and S. J. Pope, *J. Am. Chem. Soc.*, 2003, **125**, 10526–10527.
- 19 T. J. Sorensen, M. Tropicano, O. A. Blackburn, J. A. Tilney, A. M. Kenwright and S. Faulkner, *Chem. Commun.*, 2013, **49**, 783–785.
- 20 T. J. Sorensen and S. Faulkner, *Acc. Chem. Res.*, 2018, **51**, 2493–2501.
- 21 M. S. Tremblay and D. Sames, *Chem. Commun.*, 2006, 4116–4118.
- 22 L. S. Natrajan, A. J. Villaraza, A. M. Kenwright and S. Faulkner, *Chem. Commun.*, 2009, 6020–6022.
- 23 M. P. Placidi, A. J. Villaraza, L. S. Natrajan, D. Sykes, A. M. Kenwright and S. Faulkner, *J. Am. Chem. Soc.*, 2009, **131**, 9916–9917.
- 24 L. Tei, G. Gugliotta, S. Avedano, G. B. Giovenzana and M. Botta, *Org. Biomol. Chem.*, 2009, **7**, 4406–4414.
- 25 D. J. Lewis, P. B. Glover, M. C. Solomons and Z. Pikramenou, *J. Am. Chem. Soc.*, 2011, **133**, 1033–1043.
- 26 J. J. Le Roy, J. Cremers, I. A. Thomlinson, M. Slota, W. K. Myers, P. H. Horton, S. J. Coles, H. L. Anderson and L. Bogani, *Chem. Sci.*, 2018, **9**, 8474–8481.
- 27 J. D. Dunitz and A. Gavezzotti, *Acc. Chem. Res.*, 1999, **32**, 677–684.
- 28 C. R. Martinez and B. L. Iverson, *Chem. Sci.*, 2012, **3**, 2191–2201.
- 29 H. Takezawa and M. Fujita, *Bull. Chem. Soc. Jpn.*, 2021, **94**, 2351–2369.
- 30 O. Guillou, C. Daiguebonne, G. Calvez and K. Bernot, *Acc. Chem. Res.*, 2016, **49**, 844–856.
- 31 H. Q. Yin and X. B. Yin, *Acc. Chem. Res.*, 2020, **53**, 485–495.
- 32 J. P. Costes, F. Dahan, A. Dupuis, S. Lagrave and J. P. Laurent, *Inorg. Chem.*, 1998, **37**, 153–155.
- 33 S. Tamburini, S. Sitran, V. Peruzzo and P. A. Vigato, *Eur. J. Inorg. Chem.*, 2009, 155–167.
- 34 X. Y. Chen, Y. Bretonniere, J. Pecaut, D. Imbert, J. C. Bunzli and M. Mazzanti, *Inorg. Chem.*, 2007, **46**, 625–637.
- 35 D. Aguila, L. A. Barrios, V. Velasco, O. Roubeau, A. Repollès, P. J. Alonso, J. Sesé, S. J. Teat, F. Luis and G. Aromi, *J. Am. Chem. Soc.*, 2014, **136**, 14215–14222.
- 36 J. Gonzalez-Fabra, N. A. G. Bandeira, V. Velasco, L. A. Barrios, D. Aguila, S. J. Teat, O. Roubeau, C. Bo and G. Aromi, *Chem. – Eur. J.*, 2017, **23**, 5117–5125.
- 37 D. Aguila, V. Velasco, L. A. Barrios, J. Gonzalez-Fabra, C. Bo, S. J. Teat, O. Roubeau and G. Aromi, *Inorg. Chem.*, 2018, **57**, 8429–8439.
- 38 E. Macaluso, M. Rubin, D. Aguila, A. Chiesa, L. A. Barrios, J. I. Martinez, P. J. Alonso, O. Roubeau, F. Luis, G. Aromi and S. Carretta, *Chem. Sci.*, 2020, **11**, 10337–10343.
- 39 D. Maniaki, D. Garay-Ruiz, L. A. Barrios, D. O. T. A. Martins, D. Aguila, F. Tuna, D. Reta, O. Roubeau, C. Bo and G. Aromi, *Chem. Sci.*, 2022, **13**, 5574–5581.
- 40 D. Maniaki, A. Sickinger, L. A. B. Moreno, D. Aguila, O. Roubeau, N. S. Settineri, Y. Guyot, F. Riobe, O. Maury, L. A. Galan and G. Aromi, *Inorg. Chem.*, 2023, **62**, 3106–3115.
- 41 *Spectroscopic Properties of Rare Earths in Optical Materials*, ed. R. Hull, J. Parisi, R. M. O. Osgood, H. Warlimont, G. Liu and B. Jacquier, Springer Series in Materials Science, Springer Berlin, Heidelberg, 2005.
- 42 G. Chem, H. Qiu, P. N. Prasad and X. Chen, *Chem. Rev.*, 2014, **114**, 5161–5214.
- 43 B. Z. Zheng, J. Y. Fan, B. Chen, X. Qin, J. Wang, F. Wang, R. R. Deng and X. G. Liu, *Chem. Rev.*, 2022, **122**, 5519–5603.
- 44 K. A. White, D. A. Chengelis, K. A. Gogik, J. Stehman, N. L. Rosi and S. Petoud, *J. Am. Chem. Soc.*, 2009, **131**, 18069–18071.
- 45 H. Q. Yin and X. B. Yin, *Acc. Chem. Res.*, 2020, **53**, 485–495.



- 46 S. Comby, R. Scopelliti, D. Imbert, L. J. Charbonnière, R. Ziessel and J.-C. G. Bünzli, *Inorg. Chem.*, 2006, **45**, 3158–3160.
- 47 D. A. Galico, A. A. Kitos, J. S. Ovens, F. A. Sigoli and M. Murugesu, *Angew. Chem., Int. Ed.*, 2021, **60**, 6130–6136.
- 48 R. C. Knighton, L. K. Soro, L. Frances-Soriano, A. Rodriguez-Rodriguez, G. Pilet, M. Lenertz, C. Platas-Iglesias, N. Hildebrandt and L. J. Charbonniere, *Angew. Chem., Int. Ed.*, 2022, **61**, e202113114.
- 49 D. A. Galico, C. M. S. Calado and M. Murugesu, *Chem. Sci.*, 2023, **14**, 5827–5841.
- 50 T. D. Ladd, F. Jelezko, R. Laflamme, Y. Nakamura, C. Monroe and J. L. O'Brien, *Nature*, 2010, **464**, 45–53.
- 51 R. D. Shannon, *Acta Crystallogr., Sect. A: Cryst. Phys., Diffraction, Theor. Gen. Crystallogr.*, 1976, **32**, 751–767.
- 52 P. E. Ryan, G. Canard, S. Koeller, B. Bocquet and C. Piguet, *Inorg. Chem.*, 2012, **51**, 10012–10024.
- 53 S. Koeller, G. Bernardinelli, B. Bocquet and C. Piguet, *Chem. – Eur. J.*, 2003, **9**, 1062–1074.
- 54 S. Koeller, G. Bernardinelli and C. Piguet, *Dalton Trans.*, 2003, 2395–2404.
- 55 G. Canard, S. Koeller, G. Bernardinelli and C. Piguet, *J. Am. Chem. Soc.*, 2008, **130**, 1025–1040.
- 56 M. Borkovec, J. Hamacek and C. Piguet, *Dalton Trans.*, 2004, 4096–4105.
- 57 T. Riis-Johannessen, G. Bernardinelli, Y. Filinchuk, S. Clifford, N. Dalla-Favera and C. Piguet, *Inorg. Chem.*, 2009, **48**, 5512–5525.
- 58 C. Piguet, G. Bernardinelli, B. Bocquet, A. Quattropiani and A. F. Williams, *J. Am. Chem. Soc.*, 1992, **114**, 7440–7451.
- 59 C. Piguet, J.-C. G. Bünzli, G. Bernardinelli, G. Hopfgartner, S. Petoud and O. Schaad, *J. Am. Chem. Soc.*, 1996, **118**, 6681–6697.
- 60 J.-M. Bénech, C. Piguet, G. Bernardinelli, J.-C. G. Bünzli and G. Hopfgartner, *J. Chem. Soc., Dalton Trans.*, 2001, 684–689.
- 61 L. Aboshyan-Sorgho, T. Lathion, L. Guenee, C. Besnard and C. Piguet, *Inorg. Chem.*, 2014, **53**, 13093–13104.
- 62 J. Hamacek, *Metallofoldamers, Supramolecular Architectures from Helicates to Biomimetics*, ed. G. Maayan and M. Albrecht, John Wiley Sons, Ltd, Chichester, 2013, ch. 3, pp. 91–123.
- 63 J. Hamacek, S. Blanc, M. Elhabiri, E. Leize, A. van Dorsselaer, C. Piguet and A. M. Albrecht-Gary, *J. Am. Chem. Soc.*, 2003, **125**, 1541–1550.
- 64 M. L. Connolly, *J. Am. Chem. Soc.*, 1985, **107**, 1118–1124.
- 65 C. Piguet, J.-C. G. Bünzli, G. Bernardinelli, G. Hopfgartner and A. F. Williams, *J. Am. Chem. Soc.*, 1993, **115**, 8197–8206.
- 66 N. Martin, J.-C. G. Bünzli, V. McKee, C. Piguet and G. Hopfgartner, *Inorg. Chem.*, 1998, **37**, 577–589.
- 67 S. Floquet, N. Ouali, B. Bocquet, G. Bernardinelli, D. Imbert, J.-C. G. Bünzli, G. Hopfgartner and C. Piguet, *Chem. – Eur. J.*, 2003, **9**, 1860–1875.
- 68 K. Zeckert, J. Hamacek, J.-M. Senegas, N. Dalla Favera, S. Floquet, G. Bernardinelli and C. Piguet, *Angew. Chem., Int. Ed.*, 2005, **44**, 7954–7958.
- 69 D. Casanova, J. Cirera, M. Llunell, P. Alemany, D. Avnir and S. Alvarez, *J. Am. Chem. Soc.*, 2004, **126**, 1755–1763.
- 70 S. Alvarez, *Dalton Trans.*, 2005, 2209–2233.
- 71 E. Cremades, J. Echeverria and S. Alvarez, *Chem. – Eur. J.*, 2010, **16**, 10380–10396.
- 72 A. Ruiz-Martinez, D. Casanova and S. Alvarez, *Dalton Trans.*, 2008, 2583–2591.
- 73 A. Ruiz-Martinez, D. Casanova and S. Alvarez, *Chem. – Eur. J.*, 2008, **14**, 1291–1303.
- 74 M. Seitz, A. G. Oliver and K. N. Raymond, *J. Am. Chem. Soc.*, 2007, **129**, 11153–11160.
- 75 R. B. Jordan, *Inorg. Chem.*, 2023, **62**, 3715–3721.
- 76 A. Trzesowska, R. Kruszynski and T. J. Bartczak, *Acta Crystallogr., Sect. B: Struct. Sci.*, 2004, **60**, 174–178.
- 77 A. Trzesowska, R. Kruszynski and T. J. Bartczak, *Acta Crystallogr., Sect. B: Struct. Sci.*, 2005, **61**, 429–434.
- 78 A. Trzesowska, R. Kruszynski and T. J. Bartczak, *Acta Crystallogr., Sect. B: Struct. Sci.*, 2006, **62**, 745–753.
- 79 I. D. Brown, *Chem. Rev.*, 2009, **109**, 6858–6919.
- 80 C. Piguet and J.-C. G. Bünzli, in *Handbook on the Physics and Chemistry of Rare Earths*, ed. K. A. Gschneidner Jr, J.-C. G. Bünzli and V. K. Pecharsky, Elsevier Science, Amsterdam, 2010, vol. 40, pp. 301–553.
- 81 G. Koper and M. Borkovec, *J. Phys. Chem. B*, 2001, **105**, 6666–6674.
- 82 J. Hamacek, M. Borkovec and C. Piguet, *Dalton Trans.*, 2006, 1473–1490.
- 83 K. Zeckert, J. Hamacek, J.-P. Rivera, S. Floquet, A. Pinto, M. Borkovec and C. Piguet, *J. Am. Chem. Soc.*, 2004, **126**, 11589–11601.
- 84 S. Petoud, J.-C. G. Bünzli, F. Renaud, C. Piguet, K. J. Schenk and G. Hopfgartner, *Inorg. Chem.*, 1997, **36**, 5750–5760.

